Article

In-situ X-ray scattering observation of colloidal epitaxy at the gas-liquid-solid interface

Xiao Wang[1,2], Zhi Qiao[1,2], Zhu Fang[1,2], Yufeng Zhai[1,2], Runze Yu[1,2] & Gang Chen [1] ✉

The convective self-assembly of dip-coating is a long-established technique widely employed in scientific and industrial applications. Despite its apparent importance, many of the fundamental aspects remain unknown, particularly the exact assembling mechanism and its relationship with evaporation kinetics and fluid dynamics. Here, we perform the in-situ small-angle X-ray scattering study of the real-time convective self-assembly of colloidal particles inside a meniscus. This approach allows us to resolve the transient assembling processes occurring at the gas, liquid and solid interfaces. Together with ex-situ scanning electron microscopy measurements via the freeze-dry method, the colloidal epitaxy process is uncovered, where the multilayer is sequentially assembled using the interfacial monolayer as a template. The microscopic ordering of the final multilayer is highly correlated with that of the initial monolayer. The evaporation kinetics and fluid dynamics are numerically simulated, which rationalizes the monolayer formation and the dynamic epitaxial process.

The ability to assemble colloidal crystals on smooth substrates has enabled a wide range of applications, including optoelectronics[1,2], electrochemistry[3], and biosensing[4], and provided templates for ordered porous materials[5]. The convective self-assembly method of dip-coating has attracted broad interests as a potential technique for the quick and low-cost assembly of large and continuous colloidal films with ordered nanostructures. In dip-coating, a meniscus rises up when a substrate is immersed in a colloidal suspension. As the substrate withdraws and solvent evaporates, colloidal particles assemble in the vicinity of the three-phase contact line where vapor, solvent, and substrate meet. A series of structures and patterns, such as stripes[6,7], arrays[8,9], monolayers, and multilayers[5,10], are generated through dip-coating. To form large-area, highly ordered colloidal crystals in a controllable and tunable manner has been an intriguing subject of research over the past decade[11,12].

The hard-sphere-like colloidal particles tend to form face-centered cubic (fcc) or hexagonal close-packed (hcp) structures during the liquid-to-solid transition[13]. Unlike traditional colloidal crystallization in bulk solutions, convective self-assembly achieves ordering without reaching thermodynamic equilibrium. In this dynamic assembly process, several critical factors, such as particle concentration, withdrawal velocity, evaporation rate, solvent flow, and liquid viscosity, play significant roles. Currently, most studies are carried out in the regime of small capillary number where the classical Landau-Levich law follows and focused on the film entrainment thickness[14,15] and morphology[16]. However, the exact assembling mechanism at the gas-liquid-solid interfaces and the kinetic pathways of colloidal particles inside the meniscus remain elusive.

The impediment is partially ascribed to the limited tools available to track the dynamic dip-coating process. It is usually investigated by optical microscopy, whereas popular methods, such as electron microscopy and atomic-force microscopy, become incompetent to a liquid system. The finite field depth of a microscope objective also makes it intractable to probe the internal structure of a colloidal

[1]School of Physical Science and Technology, ShanghaiTech University, Shanghai, China. [2]These authors contributed equally: Xiao Wang, Zhi Qiao, Zhu Fang, Yufeng Zhai, Runze Yu. ✉e-mail: gchen@shanghaitech.edu.cn
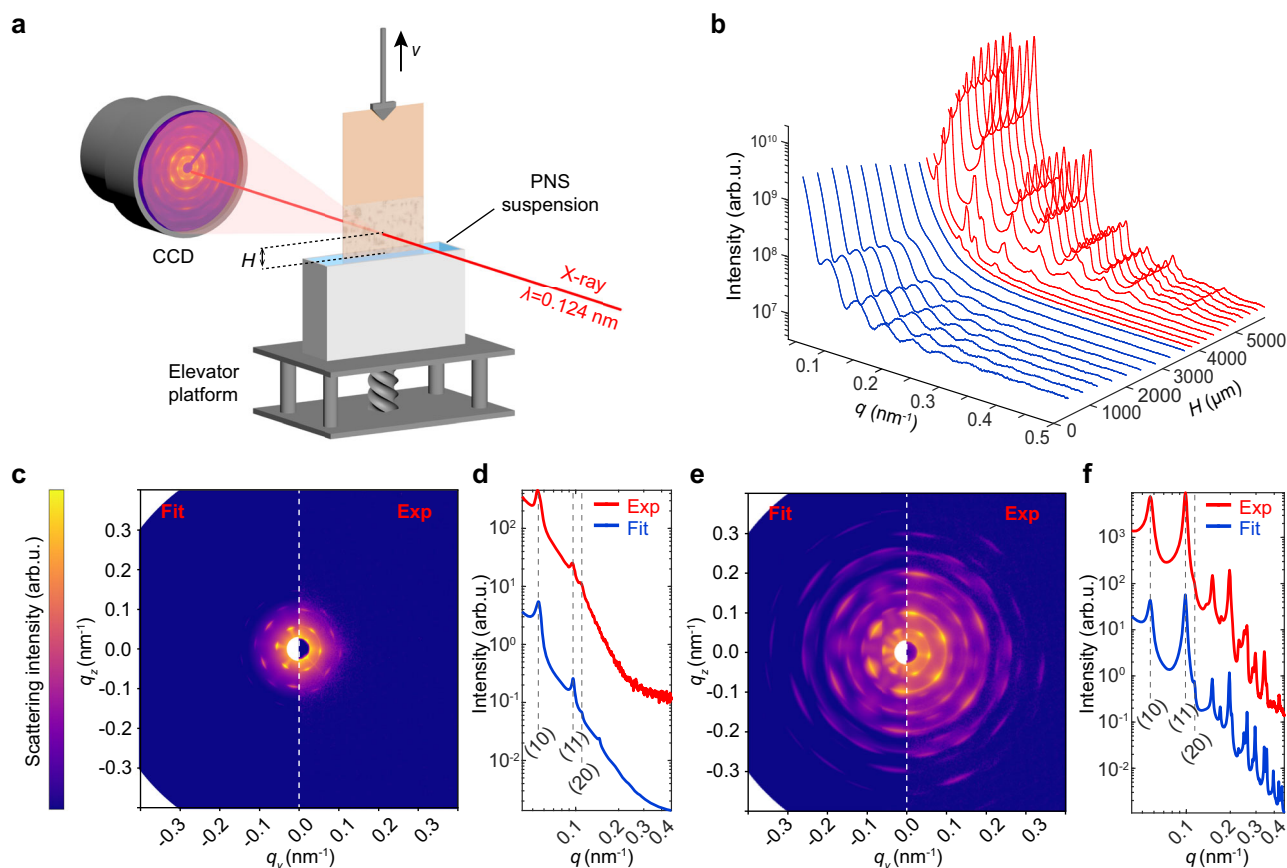
Fig. 1 | Schematic representation of the in-situ SAXS setup and the experimental and fitting results. a X-ray beam from the synchrotron radiation scatters from a colloidal film on a dip coater sitting on an elevator platform. **b** Height-resolved 1D SAXS curves obtained by integrating the 2D scattering patterns taken during the dip-coating process. The blue and red curves are recorded in the liquid and assembling regions, respectively. **c**, **d** The 2D experimental and simulated SAXS patterns of the PS NS monolayer obtained at $H = 3800$ μm. The 1D SAXS curves are obtained by integrating the 2D scattering patterns. **e**, **f** The 2D experimental and simulated SAXS patterns of the dried multilayer obtained at $H = 5800$ μm. The 1D SAXS curves are obtained by integrating the 2D scattering patterns. Source data are provided as a Source Data file.

assembly. Here, we report the in-situ small-angle X-ray scattering (SAXS) study of the real-time convective self-assembly process of polystyrene nanospheres (PS NSs) at the gas, liquid, and solid interfaces. Together with ex-situ scanning electron microscopy (SEM) measurements employing the freeze-dry method, the colloidal epitaxy process is uncovered. It reveals that the multilayer is sequentially assembled using the interfacial monolayer as a template. The ordering of the resultant multilayer is highly correlated with that of the initial monolayer. The evaporation and fluid dynamics simulations elucidate the kinetic pathways of the colloidal particles inside the meniscus, which rationalizes the monolayer formation and the dynamic epitaxial process. Guided by the epitaxial assembling mechanism, the microscopic ordering of the colloidal film is improved by tuning the environmental temperature to refine the quality of the interfacial monolayer.

Results

In-situ SAXS measurements

The in-situ SAXS measurements are conducted on the PS NS films deposited on mica plates. As shown in Fig. 1a, the mica plate is immersed about 30 mm deep into a container filled with the 1.67 vol.% PS NS solution and then lifted by a dip coater at a constant speed of 0.1 mm min^{-1}. The contact angle between the mica plate and the PS NS solution is measured and shown in Supplementary Fig. 1. The synchrotron X-ray beam is aimed at the vertical central axis of the mica plate and the whole dip-coating instrument is supported by an elevator

platform. During the PS NS dip-coating process, the elevator platform is controlled to adjust the relative height (H) between the X-ray illuminated spot on mica plate and the top liquid surface. The two-dimensional (2D) SAXS patterns are recorded at different H values by a CCD detector (the acquisition time is 300 s for H less than 5000 μm and 100 s for H greater than 5000 μm). The environmental temperature and relative humidity (RH) are controlled to be 27 ± 1 °C and $55\% \pm 5\%$, respectively.

The normalized one-dimensional (1D) X-ray scattering curves obtained by averaging along the azimuthal direction of the 2D SAXS patterns are shown in Fig. 1b. They can be divided into two regions as marked with different colors. At the liquid phase region, the X-ray scattering signal mainly comes from the summation of single particle scattering. By fitting the initial 1D SAXS curve, the diameter of PS NSs is found to be 134.1 nm with the polydispersity of ≈1.8% (see Supplementary Fig. 2). The scattering intensity decreases as H increases since the meniscus thickness decreases along the same direction. At the assembling region, the intensities of the emerging Bragg peaks rapidly rise and then stabilize. At $H = 3800$ μm, the starting point of the assembling region, three Bragg peaks appear in the 1D curves at $q = 0.054, 0.094$ and 0.108 nm^{-1}, which match the 2D hexagonal lattice planes with the Miller indices of (10), (11) and (20). It suggests that a 2D hexagonal monolayer firstly forms at the air/water interface. As shown in Fig. 1c, d, the distinct Bragg spots in the 2D scattering patterns demonstrate the monolayer is highly ordered. The scattering patterns simulated under the decoupling approximation employing the
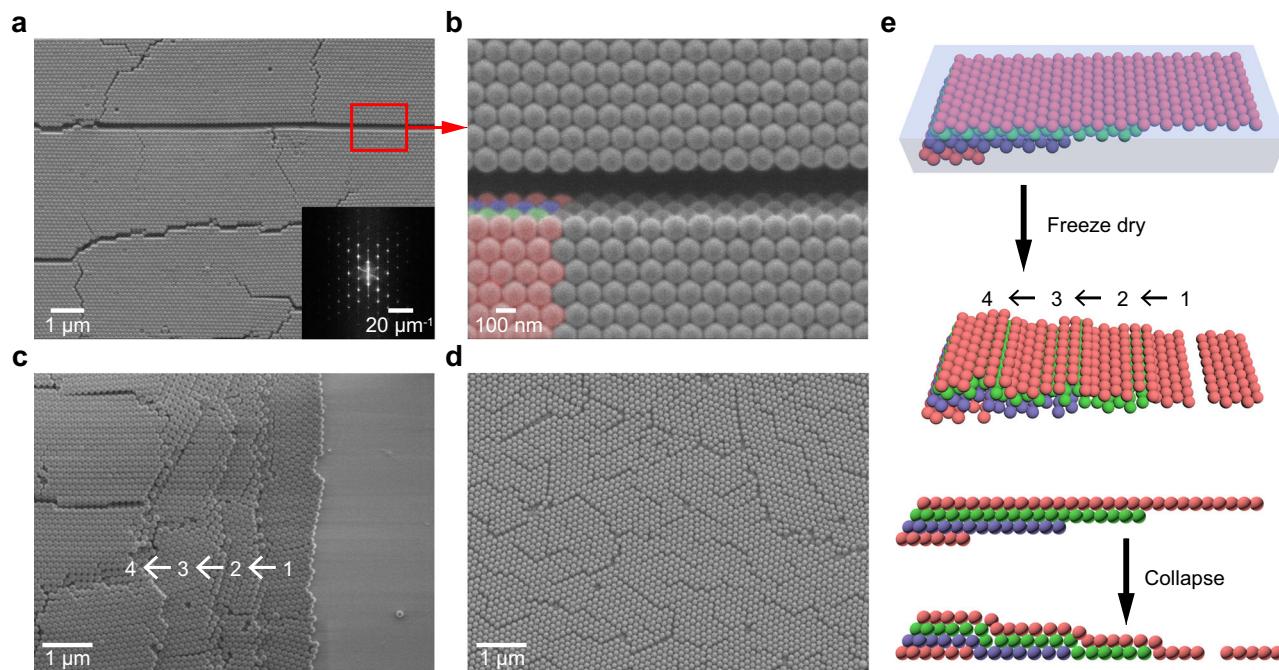
Fig. 2 | Ex-situ SEM measurements of the colloidal films. a, b SEM images of the PS NS film on a mica substrate. The inset shows the Fourier transform pattern. The different hexagonal lattice planes are marked with distinct colors: A (red), B (green), and C (blue). The 4-layer fcc-type stacking of *ABCA* is shown in (**b**). **c** SEM image of the step-like assembling front and the number of layers is marked. **d** SEM image of the monolayer near the assembling front. **e** Schematic diagrams for the collapsing of the step-like assembling front during ice sublimation. The colors correspond to those in (**b**).

structural model of a 2D hexagonal monolayer show high consistency with the experimental SAXS patterns. Subsequently, the dewetting process is observed, which causes the rapid rise of the scattering intensity. In the meantime, the intensity of the (11) peak becomes higher than that of the (10) peak. It implies the PS NS multilayer is encountered at this period. A series of 1D scattering profiles for the hexagonally stacked multilayers of different layer numbers are simulated in Supplementary Fig. 3. For the dried film recorded at $H = 5800$ µm, the model of a 4-layer fcc-type stacking with the lattice constant of 127.2 nm provides the best fits to the experimental data as shown in Fig. 1e, f.

Ex-situ SEM measurements

When the PS NSs are completely dry, a translucent film is formed (see Supplementary Fig. 4). The microscopic structure of the dried film is characterized by the SEM measurements. As shown in Fig. 2a, the film is composed of highly ordered PS NS assemblies with a uniform thickness and cracks at the grain boundaries[17]. The Fourier transform of the SEM image in the inset of Fig. 1a demonstrates the PS NS film has the long-range hexagonally ordered structure. Zoom in along a crack to view the cross-section (Fig. 2b), we find the film is mainly constituted by the 4-layer fcc-type (*ABCA*) hexagonal stacking superlattice. The stacking model is given in Supplementary Fig. 5. The PS NSs show good monodispersity in sizes and the lattice constant is measured to be 126.8 nm, consistent with the SAXS result.

While the in-situ X-ray scattering experiment unveils the monolayer-to-multilayer transition, the detailed assembling behavior at the forefront is still unknown. We perform ex-situ SEM measurements employing the freeze-dry method through liquid nitrogen cooling followed by ice sublimation[18]. Briefly, in the course of dip-coating, the mica plate is quickly pulled out of the PS NS solution, soaked into liquid nitroge,n and then installed in a −2 °C refrigerator for ice sublimation. As shown in Fig. 2c, a clear step-like assembling front is observed. The transition length from monolayer to 4-layer is ≈3 µm, indicating a transient epitaxial assembling process. It is well

known that the convection-induced colloidal assembly takes place at the air/water interface[19,20]. We also find the large-size PS NS monolayer away from the assembling front in low magnification SEM image (Supplementary Fig. 6). As shown in Fig. 2d, the PS NS monolayer exhibits the hexagonally ordered structure. It indicts the monolayer might be teared off when the mica plate is lifted out of solution. Based on the ex-situ assembling front profile, we can conjecture the actual assembling front in solution as schematically illustrated in Fig. 2e. When the ice is sublimated, the monolayer and the step-like assembling front will collapse, which causes dislocations at the layer-number-change region and forms the square-packing PS NSs. The square-packing structure is commonly found in the transition region where fcc lattice changes layer numbers[21].

Dynamic assembling process

To gain more insights into the dynamic assembling process of dip-coating, we carry out detailed analyses of the in-situ SAXS data. The integrated 1D X-ray scattering curves recorded in the assembling region are shown in Fig. 3a. The thickness of the meniscus T can be estimated from the X-ray beam attenuation caused by water absorption (Fig. 3b). The variance in T, when considering the difference in absorption between water and PS NSs, is negligible (Supplementary Note 1). We find the monolayer first appears at $H = 3800$ µm where the liquid meniscus thickness is about 4 µm. In the assembling region, the scattering intensity rapidly rises and stabilizes. Meanwhile, the (10) Bragg peak is shifted from $q = 0.054$ to 0.056 nm^{-1}, indicating the shrinkage of the lattice constant. The interparticle distance of the PS NS assembly is estimated by fitting the SAXS curves, and the PS NS diameter in the liquid phase region is fitted by the scattering model of spheres (Fig. 3c). The total scattering power can be obtained from the SAXS intensity $I(q)$ through the expression $Q = \int I(q)q^2 dq$ (Fig. 3d). In the dewetting process, the residue water in the interstices of the PS NS assembly evaporates away. X-ray scattering signal arises from the density difference between PS NS and air instead of water, so the overall scattering contrast increases substantially. The dewetting
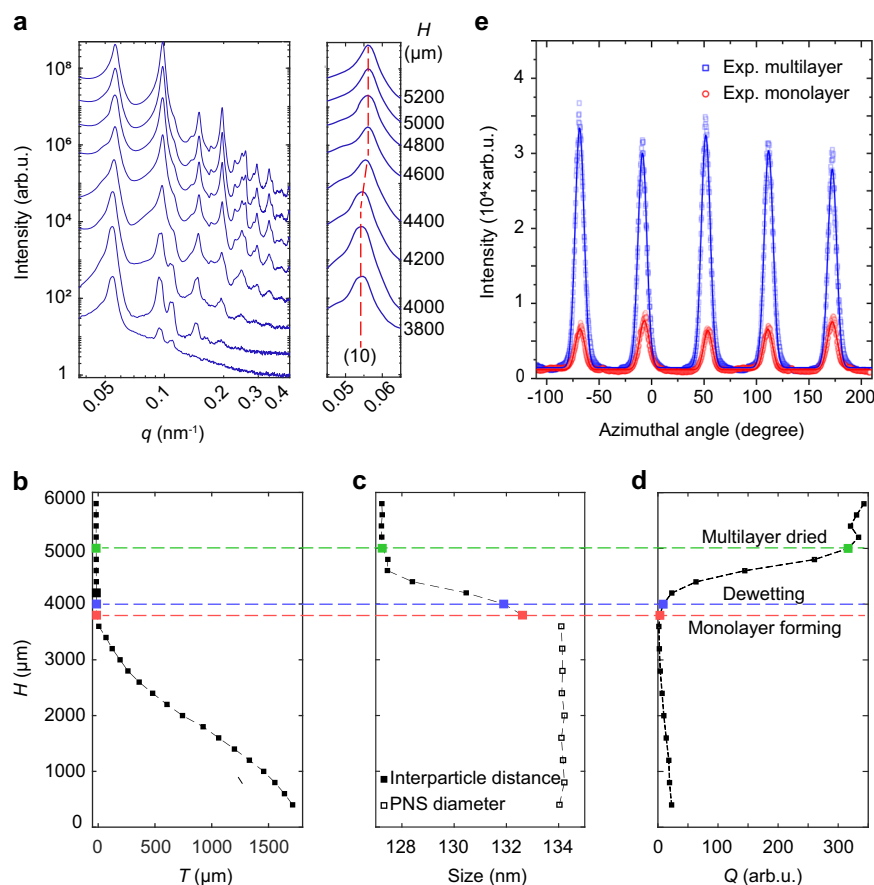
Fig. 3 | Detailed analyses of the in-situ SAXS data. a 1D SAXS curves recorded at the assembling region. The central positions of the (10) peaks shift towards higher *q*. **b**–**d** The height-resolved meniscus thickness *T*, the total scattering power $Q = \int I(q)q^2dq$ and the PS NS particle size. The colored dashed lines indicate the starting points of different stages: monolayer forming (red), dewetting (blue), multilayer dried (green). **e** Azimuthal intensities plotted along the (10) scattering ring for the monolayer (red circles, *H* = 3800 μm, the intensity is quintupled for clarity) and the dried multilayer (blue circles, *H* = 5800 μm). The solid lines are the Gaussian peak fittings. Source data are provided as a Source Data file.

process initiates when Q starts to increase as shown in Fig. 3d, which corresponds to *H* = 4000 μm in Fig. 3b. The PS NS film is totally dried when *Q* begins to flatten and the interparticle distance stays invariant, which corresponds to *H* = 5000 μm. Based on these results, we conclude the assembling process as follows: for *H*<3800 μm, the diameter of the PS NSs stays unvaried (≈134.1 nm) and *Q* decreases due to the meniscus thickness and particle number decreases (Supplementary Fig. 7); at *H* = 3800 μm, the starting point of the assembling region, the PS NSs assemble into an interfacial monolayer; for *H*>4000 μm, the dewetting process begins and a continuous decrease of the lattice constant is observed, from 132.6 nm for the monolayer to 127.2 nm for the dried multilayer. It implies that the cracks observed in the SEM images of the dried films are likely originated from the lattice shrinkage during the dewetting process.

The in-situ SAXS and ex-situ SEM results have revealed an ordered monolayer is first formed at the air/water interface and followed by a transient epitaxy process. To evaluate the correlation of the structural ordering between the initial monolayer and the final multilayer, we compare the angular orientational distributions of their SAXS patterns. As shown in Fig. 3e, the scattering intensities along the Debye-Scherrer rings of the (10) planes of the initial monolayer (Fig. 1c) and the dried multilayer (Fig. 1e) are integrated and plotted against the azimuthal angle. The peak positions and full width at half maxima (FWHMs) of the peaks are nearly identical as acquired from the Gaussian peak fittings (the average FWHMs are 10.0° for the monolayer and 10.5° for the multilayer), implying that the multilayer is epitaxially stacked using the ordered monolayer as a template. This correlation indicates that the

ordering of the multilayer depends on the quality of the ordered monolayer. It is noteworthy that the orientation degree is not affected by the lattice shrinkage. Combined with the SEM results, we speculate that the shrinkage-induced cracks are formed at the grain boundaries.

In the dewetting process, the X-ray scattering signal arises from the scattering length density difference between PS NS (1.06 g mL⁻¹) and air (0.001 g mL⁻¹) instead of water (1 g mL⁻¹), so the overall scattering contrast increases by ≈300 times. The SAXS signal is mainly originated from the dried section of the film at this stage. We find the intensity of the second Bragg peak ascribed to the (11) planes raises gradually, implying that the number of the dried layers increases. At *H* = 4200 μm, both the 2D SAXS pattern and the 1D curve are highly consistent with those simulated for the monolayer (Fig. 4a). At *H* = 4400 μm, the 2D SAXS pattern and the 1D curve can be fitted by the mixture layer of 28% monolayer and 72% 2-layer (Fig. 4b). At *H* = 4600 μm, the scattering signals agree well with the mixture layer of 68% 2-layer and 32% 3-layer (Fig. 4c). At *H* = 4800 μm, the scattering signals of the multilayer are consistent with those of the 4-layer (Fig. 4d). The parameters used in the X-ray scattering fittings, including the lattice constant, the radial and azimuthal peak widths, are listed in Supplementary Table 1.

Evaporation and fluid dynamics simulations

In the assembling process, the PS NS colloids are transported from bulk liquid to the assembling front. This process is driven by the evaporation-induced liquid convective flow in the meniscus. To understand the epitaxy growth mechanism, it is essential to elucidate
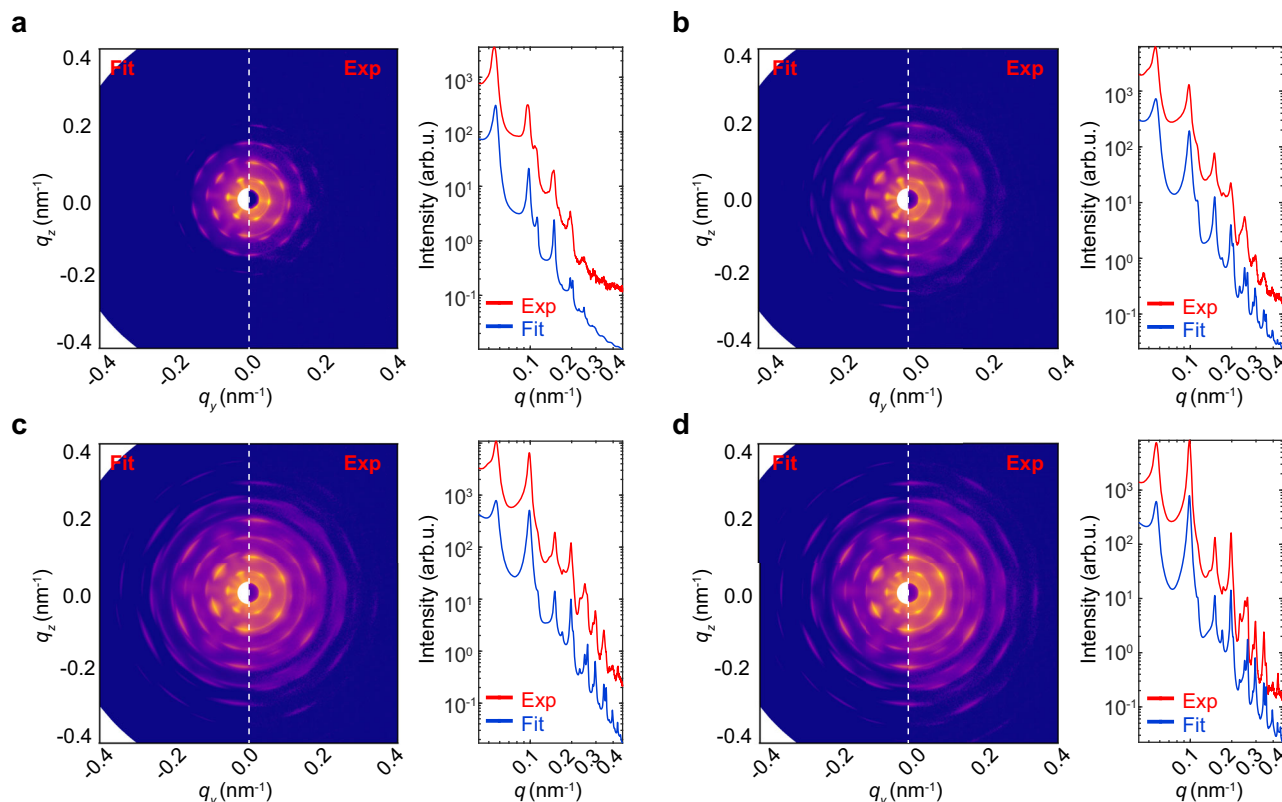
Fig. 4 | Theoretical simulations of the 2D SAXS patterns and 1D curves (also see Supplementary Fig. 8) acquired in the dewetting process. The H values are **a** 4200, **b** 4400, **c** 4600, and **d** 4800 μm, respectively. The experimental 2D SAXS patterns are compared with the corresponding simulated patterns. The experimental (red lines) and simulated (blue lines) 1D SAXS curves are extracted by integrating the corresponding 2D SAXS patterns. Source data are provided as a Source Data file.

the evaporation and convection processes. Since the meniscus profile and the environmental temperature and RH are specified, the spatial vapor concentration $\phi(r)$ can be simulated using the steady-state diffusion equation $\nabla^2\phi(r) = 0$. Subsequently, the spatial evaporation flux $J(r) = -D\nabla\phi(r)$ can be computed as shown in Fig. 5a, where D is the vapor diffusion coefficient. $J(r)$ at a specific H of the air/water interface is defined as the interfacial evaporation rate $F(H)$, as shown in Fig. 5b. As previously found in the coffee-ring effect[21], the evaporation rate is maximum at the contact line. $F(H)$ can be fitted by the theoretical relation derived by Deegan et al.[22] as $F(H) = a(5000 - h)^b$, where h is the dimensionless value of H. For the contact line located at $H = 5000$ μm, we find $a = 0.1421$ mol m^{-2} s and $b = -0.4853$. The fitted b is consistent with the theoretical value of -0.5 for a small contact angle.

The PS NSs can be transported through the convective flow. Given the long timescale of Brownian motion, the PS NSs can be regarded as solutes that travel along the stream lines in the fluid[23]. Based on the meniscus profile, water viscosity, withdrawal velocity, and the flow velocity across the air/water interface determined from the evaporation simulation, the fluid dynamics inside the meniscus can be simulated employing the Navier–Stokes equations[22]. The flow velocity and the stream lines are shown in Fig. 5a, and the average flow velocity $\bar{v}$ at different H is calculated and plotted in Fig. 5c. As can be seen, $\bar{v}$ increases dramatically as the meniscus thickness decreases, so there is an acceleration in the flow velocity towards the assembling front. At $H = 3800$ μm, where the monolayer first appears, $\bar{v}$ is estimated to be ≈40 μm s^{-1}. Therefore, the moving velocity of PS NSs at the assembling front is much faster than the mica withdrawal velocity of 1.67 μm s^{-1}. In the typical 2D flow configuration of the Landau-Levich type, the stream lines can be divided into laminar flow and recirculation flow regions[24]. Due to the relatively small withdrawal velocity, the recirculation flow

under the present experimental conditions is negligible (more simulation results are shown in Supplementary Fig. 9).

Overall, the dynamic epitaxial assembling and dewetting processes of PS NSs in dip-coating are schematically illustrated in Fig. 5d. An ordered monolayer is formed as the PS NSs are transported and trapped at the air/water interface. The second layer cannot easily form because of the large flow velocity and the electrostatic repulsion between PS NSs[25]. Due to the high evaporation rate at the three-phase contact line, the PS NSs are transported by the upward flow and assembled at the assembling front. A transient colloidal epitaxy occurs, where the sublayer stacks based on the template of the monolayer. Therefore, the degree of ordering between the monolayer and the final multilayer is highly correlated. The step-like assembling front suggests there is a component of velocity pointing towards the air/water interface. The dewetting process starts from inside out once the multilayer is assembled until it is fully dried[26].

Tuning the multilayer ordering

A series of the temperature-controlled dip-coating experiments are performed to optimize the ordering of the resultant multilayers. The colloidal epitaxy process is further verified by comparing the degree of ordering between the monolayers and multilayers formed at different temperatures. The mica plates are immersed into the 1.67 vol.% PS NS solution and then withdrawn at a constant speed of 0.1 mm min^{-1}. The RH is controlled to be 50% ± 5% and the environmental temperature is set at 19 ± 1, 23 ± 1, 27 ± 1, and 31 ± 1 °C, respectively. To analysis the monolayer structure, ex-situ SEM measurements are performed using the freeze-dry method. For a colloid in the hexagonal lattice, its position and the positions of its six nearest neighbors are registered by the self-developed computer code. As shown in Fig. 6a–d, the local
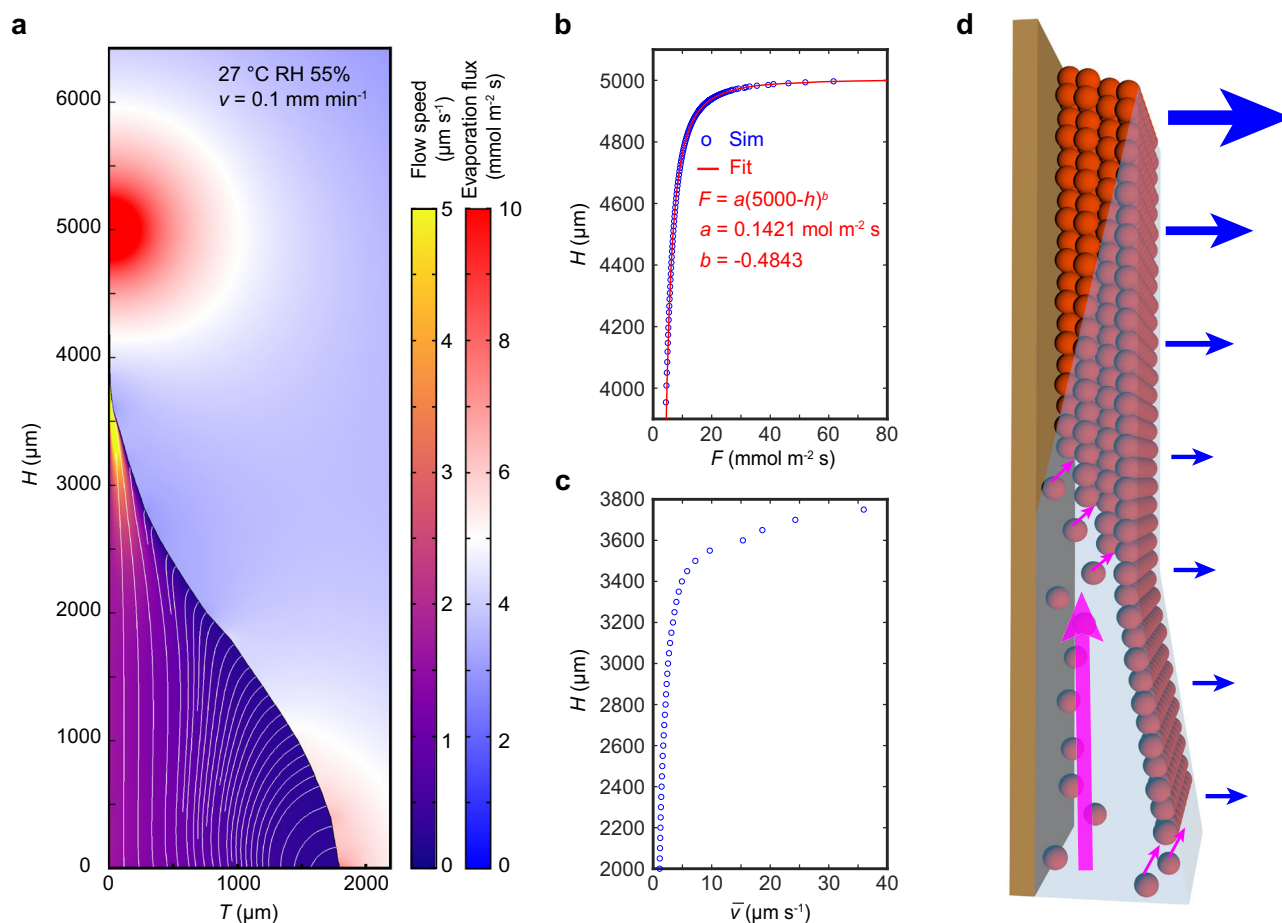
Fig. 5 | Evaporation and fluid dynamics simulations and the epitaxial assembling mechanism. a Stimulations of the evaporation (color for evaporation flux J) and fluid (color for flow velocity v, white lines for stream lines) dynamics at the temperature of 27 °C, RH of 55%, and withdrawal velocity of 0.1 mm min^{-1}. **b** The evaporation rate F obtained at different H at the air/water interface (blue circles) and the corresponding fitted results (red curve and values), where h is the

dimensionless value of H, a is in the unit of mol m^{-2} s and b is a dimensionless parameter. **c** The averaged velocity $\bar{v}$ obtained at different H. **d** Schematic diagram of the dynamic assembling process in dip-coating. The blue arrows indicate the liquid evaporation and the pink arrows indicate the PS NS motion. Source data are provided as a Source Data file.
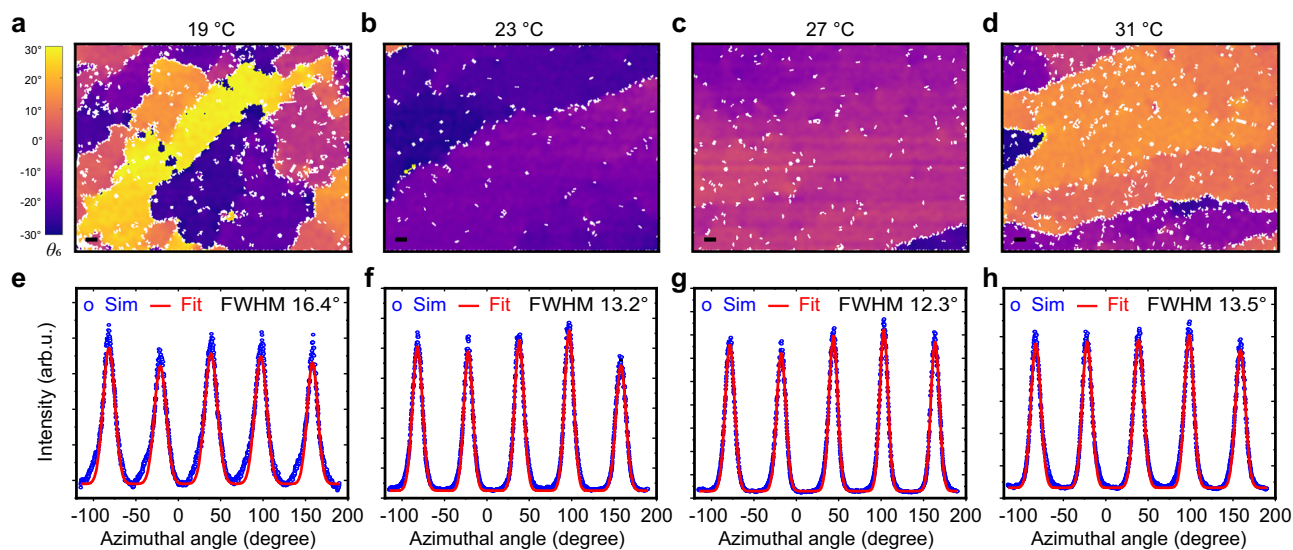

Fig. 6 | Temperature-controlled dip-coating experiments. a–d Local orientation (θ_6) analyses of the SEM images of the monolayers obtained at different temperatures. The scale bars are 1 μm. **e–h** Azimuthal intensities plotted along the (10)

scattering rings of the dried multilayers obtained at 19, 23, 27, and 31 °C, respectively. The experimental data (blue dots) are fitted by the Gaussian functions (red lines). Source data are provided as a Source Data file.

orientation parameter θ_6 is calculated to quantify the grain orientations of the monolayers[27] (see Supplementary Note 2 for details). The average grain size of the monolayer formed at 19 °C is obviously smaller than those formed at higher temperatures and the best monolayer with consistent orientations is obtained at 27 °C. The SAXS technique is employed to characterize the ordering of the dried multilayers (the 2D SAXS patterns are shown in Supplementary Fig. 10). The intensities along the Debye-Scherrer rings of the (10) plane are integrated and fitted by the Gaussian functions as shown in Fig. 6e–h. The fitting results show the average FWHMs are 16.4°, 13.2°, 12.3° and 13.5° for the PS NS multilayers formed at 19, 23, 27 and 31 °C, respectively. The smaller FWHMs of the Bragg spots indicate the higher degree of ordering of the resultant multilayer. Consistent with the SEM analyses of the monolayers, the SAXS results show the best multilayer is also formed at 27 °C. We propose that the environmental temperature will regulate the water evaporation rate and the flow velocity, which affects the PS NS assembling process and the ordering of the interfacial monolayer and further influences the final multilayer.

Discussion

In conclusion, the in-situ SAXS observation of the convective self-assembly process has enabled us to follow the structural evolution of colloidal particles at the gas, liquid, and solid interfaces and uncover the epitaxy growth mechanism. The liquid phase state, monolayer development, transient assembling and sequential dewetting processes are all encountered and elucidated. The ex-situ SEM measurements employing the freeze-dry method reveal the step-like assembling front near the three-phase contact line and a large-size monolayer straddling across the air/water interface. The ordering of the final multilayer is highly correlated with that of the initial monolayer. The evaporation and fluid dynamics simulations are performed based on the meniscus profile determined from the in-situ SAXS study. The numerical simulations indicate the evaporation rate and flow velocity are maximum at the three-phase contact line and the colloidal particles are speedily transported towards the assembling front. The temperature-controlled dip-coating experiments further confirm the correlation between the ordering of the monolayer and multilayer. The microscopic ordering of the colloidal film is improved by tuning the environmental temperature to refine the quality of the interfacial monolayer. The principles underlying the self-assembly process observed in this study are applicable to a wider range of colloidal materials, especially those with similar characteristics in terms of size, charge, and dispersion behaviors. Given the many useful, interesting, and economically important implementations of the dip-coating technique, a better understanding of the underlying assembling mechanism should contribute to developing new micro- and nanostructured films.

Methods

Materials

PS NSs dispersed in deionized (DI) water were purchased from Huge Biotechnology with the weight percentage of 5 wt.%. The PS NS solution was diluted with DI water to the volume fraction of 1.67 vol.% and ultrasonicated for 10 min before use. A thin sheet of mica ($10 \times 50 \times 0.02$ mm) cleaned by DI water and ethanol was treated by the oxygen plasma cleaner. The mica plate was lifted by a dip coater (LayerX, Kibron Inc.). The zeta potential of the PS NSs in DI water was −41.1 mV. It was measured by Zetasizer Nano from Malvern Instruments.

SAXS measurements

The SAXS measurements were conducted at the beamline BL16B1 of Shanghai Synchrotron Radiation Facility (SSRF), with the incident X-ray photon energy of 10 keV (wavelength $\lambda = 1.239$ Å). The flux of the incident X-ray beam was about 2×10^{11} photon s^{-1}, and the beam size was 0.25×0.48 mm. The sample-to-detector distance was set to 5100 mm. The 2D scattering patterns were collected by the Rayonix SX-165 CCD (Rayonix, Evanston, IL, USA) detector with 2048×2048 pixels (the pixel size of 80×80 μm). The in-house SAXS measurements were performed on the Xenocs Xeuss 2.0 system equipped with a micro-focus Cu K_α source (wavelength $\lambda = 1.54$ Å). The beam size was set to 0.35×0.35 mm. The scattering patterns were collected by the Pilatus3R 300k detector with the pixel size of 172×172 μm. The sample-to-detector distance was set to 6380 mm. The scattering signal of mica plate in air was taken as background. The 2D scattering patterns were integrated into the 1D scattering curves $I(q)$ as a function of the scattering vector q, where $q = (4\pi/\lambda)\sin(\theta/2)$, λ was the incident X-ray wavelength and θ was the scattering angle.

Simulations of X-ray scattering patterns

The theoretical method is given as reported in ref. 28,29. Briefly, in the decoupling approximation, the X-ray scattering intensity can be described as $I(\mathbf{q}) \propto \Delta\rho^2 n_p P(\mathbf{q})S(\mathbf{q})$, where $\Delta\rho$ is the density difference, n_p is the particle number density, $P(\mathbf{q})$ is the particle form factor and $S(\mathbf{q})$ is the structure factor. The form factor for sphere particles can be expressed as

$$P(\mathbf{q}) = \left\langle |F(\mathbf{q})|^2 \right\rangle = \int 9 \left[\frac{\sin(qR) - qR\cos(qR)}{q^3 R^3} \right]^2 n(R) \left(\frac{4}{3}\pi R^3 \right)^2 dR, \quad (1)$$

where the bracket $\langle \cdots \rangle$ represents the average over grains at all possible orientations and particle distributions, $n(R)$ is the size distribution function of particles. The structure factor can be expressed as[30]

$$S(\mathbf{q}) = \left[\frac{cZ(\mathbf{q})}{P(\mathbf{q})} G(\mathbf{q}) + 1 - \beta(\mathbf{q})G(\mathbf{q}) \right], \quad (2)$$

where c is a numerical constant, $\mathbf{q}$ is the wavevector transfer, $Z(\mathbf{q})$ is the lattice factor, $G(\mathbf{q})$ is the Debye-Waller factor and $\beta(\mathbf{q})$ is the fluctuation term related to the particle shape and polydispersity. The Debye-Waller factor is defined as:

$$G(\mathbf{q}) = \exp(-\sigma_D^2 a^2 q^2), \quad (3)$$

where σ_D is the relative root-mean-square displacement for a lattice of size a. The fluctuation term is defined as:

$$\beta(\mathbf{q}) = \frac{|\langle F(\mathbf{q}) \rangle|^2}{P(\mathbf{q})}, \quad (4)$$

The lattice factor is defined as:

$$Z(\mathbf{q}) = \sum_{hk} |F_u(g_{hk})|^2 L_q(\mathbf{q}, \mathbf{g}_{hk}) L_\psi(\mathbf{q}, \mathbf{g}_{hk}), \quad (5)$$

where the F_u is the effective form factor of the unit cell, the L_q and L_ψ are the radial and azimuthal peak width functions expressed as a Lorentzian function and a Gaussian function respectively, $\mathbf{g}_{hk}$ is the reciprocal lattice vector. The SAXS data analyses were carried out based on the self-developed codes in Matlab® and the detail discussion was given in Supplementary Note 3. The data were fitted through the covariance matrix adaptation evolution strategy (CMA-ES) method[31].

SEM measurements

The scanning electron microscope (SEM, JEOL JSM-7800F Prime) was used to characterize the PS NS films. The acceleration voltage of the electron was set to 1.0 kV.

Evaporation and fluid dynamics simulations

Based on a standard finite element modeling discretization of the Navier–Stokes equations, the laminar flows were simulated using COMSOL® Multiphysics. The boundary conditions based on the evaporation rate at the air/water interface are given in Supplementary Note 4.

Data availability

The data that support the findings of this study are available from the corresponding author upon request. Source data are provided with this paper.

Code availability

The code developed and used in this study is available from the corresponding author upon request.

References

1. Nelson, E. C. et al. Epitaxial growth of three-dimensionally architectured optoelectronic devices. *Nat. Mater.* **10**, 676–681 (2011).
2. Salles, P. et al. Electrochromic effect in titanium carbide MXene thin films produced by dip-coating. *Adv. Funct. Mater.* **29**, 1809223 (2019).
3. Deng, J. et al. Ambient methane functionalization initiated by electrochemical oxidation of a vanadium (V)-oxo dimer. *Nat. Commun.* **11**, 1–10 (2020).
4. Cassagneau, T. & Caruso, F. Inverse opals for optical affinity biosensing. *Adv. Mater.* **14**, 1629–1633 (2002).
5. Lu, Y. et al. Continuous formation of supported cubic and hexagonal mesoporous films by sol–gel dip-coating. *Nature* **389**, 364–368 (1997).
6. Watanabe, S. et al. Mechanism for stripe pattern formation on hydrophilic surfaces by using convective self-assembly. *Langmuir* **25**, 7287–7295 (2009).
7. Huang, J. et al. Spontaneous formation of nanoparticle stripe patterns through dewetting. *Nat. Mater.* **4**, 896–900 (2005).
8. Garcia Nunez, C. et al. Large-area self-assembly of silica microspheres/nanospheres by temperature-assisted dip-coating. *ACS Appl. Mater. Interfaces* **10**, 3058–3068 (2018).
9. Mehraeen, S. et al. Directed self-assembly of sub-10 nm particles: role of driving forces and template geometry in packing and ordering. *Langmuir* **31**, 8548–8557 (2015).
10. Dugay, J. et al. Tuning deposition of magnetic metallic nanoparticles from periodic pattern to thin film entrainment by dip coating method. *Langmuir* **30**, 9028–9035 (2014).
11. Hatton, B. et al. Assembly of large-area, highly ordered, crack-free inverse opal films. *PNAS* **107**, 10354–10359 (2010).
12. Schaffner, M. et al. Combining bottom-up self-assembly with top-down microfabrication to create hierarchical inverse opals with high structural order. *Small* **11**, 4334–4340 (2015).
13. Li, B. et al. Assembly and phase transitions of colloidal crystals. *Nat. Rev. Mater.* **1**, 15011 (2016).
14. Faustini, M. et al. Preparation of sol–gel films by dip-coating in extreme conditions. *J. Phys. Chem. C* **114**, 7637–7645 (2010).
15. Brasjen, B. J. et al. Dip- and die-coating of hydrophilic squares on flat, hydrophobic substrates. *Chem. Eng. Sci.* **158**, 340–348 (2017).
16. Gans, A. et al. Dip-coating of suspensions. *Soft Matter* **15**, 252–261 (2019).
17. Goehring, L. et al. Solidification and ordering during directional drying of a colloidal dispersion. *Langmuir* **26**, 9269–9275 (2010).
18. Jambon-Puillet, E. Stains from freeze-dried drops. *Langmuir* **35**, 5541–5548 (2019).
19. Born, P. G. Crystallization mechanisms in convective particle assembly. in *Crystallization of Nanoscaled Colloids* 51–73 (Springer, 2013).
20. Born, P. et al. Self-assembly of gold nanoparticles at the oil–vapor interface: from mono-to multilayers. *Langmuir* **30**, 13176–13181 (2014).
21. Meng, L. et al. The role of thickness transitions in convective assembly. *Nano Lett.* **6**, 2249–2253 (2006).
22. Deegan, R. D. et al. Capillary flow as the cause of ring stains from dried liquid drops. *Nature* **389**, 827–829 (1997).
23. Kraus, T. et al. Nanoparticle printing with single-particle resolution. *Nat. Nanotechnol.* **2**, 570–576 (2007).
24. Colosqui, C. E. et al. Hydrodynamically driven colloidal assembly in dip coating. *Phys. Rev. Lett.* **110**, 188302 (2013).
25. Wu, L. et al. In situ X-ray scattering observation of two-dimensional interfacial colloidal crystallization. *Nat. Commun.* **9**, 1335 (2018).
26. Wang, X. et al. Dynamic crystallization and phase transition in evaporating colloidal droplets. *Nano Lett.* **19**, 8225–8233 (2019).
27. Lavergne, F. A. et al. Anomalous grain growth in a polycrystalline monolayer of colloidal hard spheres. *Phys. Rev. X* **7**, 041064 (2017).
28. Förster, S. et al. Calculation of scattering-patterns of ordered nano- and mesoscale materials. *Adv. Colloid Interface Sci.* **163**, 53–83 (2011).
29. Forster, S. et al. Order causes secondary Bragg peaks in soft materials. *Nat. Mater.* **6**, 888–893 (2007).
30. Yager, K. G. et al. Periodic lattices of arbitrary nano-objects: modeling and applications for self-assembled systems. *J. Appl. Crystallogr.* **47**, 118–129 (2013).
31. Hansen, N. & Ostermeier, A. Completely derandomized self-adaptation in evolution strategies. *Evol. Comput.* **9**, 159–195 (2001).

Acknowledgements

Author contributions

G.C. conceived and supervised the research. X.W., Z.Q., Y.Z., and R.Y. carried out the SAXS experiments. X.W. and Z.F. analyzed the data. G.C. and X.W. wrote the manuscript. All authors discussed the results and commented on the manuscript.

Competing interests

The authors declare no competing interests.

Additional information